

Anisotropic-strain-enhanced hole mobility in GaN by lattice matching to ZnGeN₂ and MgSiN₂

Joshua Leveillee,^{1,2} Samuel Poncé,^{3,4} Nicholas L. Adamski,⁵ Chris G. Van de Walle,⁵ and Feliciano Giustino^{1,2}

¹⁾Oden Institute for Computational Engineering and Sciences, The University of Texas at Austin, Austin, Texas 78712, USA

²⁾Department of Physics, The University of Texas at Austin, Austin, Texas 78712, USA

³⁾Theory and Simulation of Materials (THEOS), École Polytechnique Fédérale de Lausanne, CH-1015 Lausanne, Switzerland

⁴⁾Institute of Condensed Matter and Nanosciences, Université catholique de Louvain, Chemin des Étoiles 8, B-1348 Louvain-la-Neuve, Belgium

⁵⁾Materials Department, University of California, Santa Barbara, California 93106-5050, USA

(*Electronic mail: fgiustino@oden.utexas.edu)

(Dated: 13 May 2022)

The key obstacle toward realizing integrated gallium nitride (GaN) electronics is its low hole mobility. Here, we explore the possibility of improving the hole mobility of GaN via epitaxial matching to II-IV nitride materials that have recently become available, namely ZnGeN₂ and MgSiN₂. We perform state-of-the-art calculations of the hole mobility of GaN using the *ab initio* Boltzmann transport equation. We show that effective uniaxial compressive strain of GaN along the [1̄100] by lattice matching to ZnGeN₂ and MgSiN₂ results in the inversion of the heavy hole band and split-off hole band, thereby lowering the effective hole mass in the compression direction. We find that lattice matching to ZnGeN₂ and MgSiN₂ induces an increase of the room-temperature hole mobility by 50% and 260% as compared to unstrained GaN, respectively. Examining the trends as a function of strain, we find that the variation in mobility is highly nonlinear; lattice matching to a hypothetical solid solution of Zn_{0.75}Ge_{0.75}Mg_{0.25}Si_{0.25}N₂ would already increase the hole mobility by 160%.

Wurtzite gallium nitride has become a fundamental semiconductor component in a variety of electronic and optical devices, including radio-frequency applications,^{1,2} power electronics,³ and light emitting diodes (LEDs).^{4–6} Many remarkable properties of GaN can be traced back to its electronic structure. As a wide-gap semiconductor with a band gap of 3.4 eV at room temperature,^{7,8} GaN can support higher voltages without experiencing field-induced breakdown when compared with Si. GaN can be alloyed with other nitride semiconductors such as AlN^{9,10} and InN^{11,12} to tune the band gap between 0.6 and 6.2 eV, allowing for the realization of an array of materials for optoelectronic applications.

Electrons in GaN exhibit high room-temperature mobility, reaching up to 1000 cm²/Vs^{13–19} at low defect concentration. Conversely, hole carriers in GaN exhibit comparatively low mobility, usually below 31 cm²/Vs.^{20–25} The imbalance between electron and hole mobility hinders the application of GaN to integrated electronics based on complementary field-effect devices, and severely limits the uses of *p*-channel GaN in power electronics and radio-frequency switching.^{3,26} In order to meet these technological demands, materials engineering approaches aimed at increasing the hole mobility of GaN are needed.

A common approach to improving the carrier mobility of semiconductors is via strain engineering. In the case of GaN, several experimental and theoretical/computational reports explored this possibility. Using $\mathbf{k} \cdot \mathbf{p}$ perturbation theory, Suzuki *et al.* found that compressive uniaxial strain along the in-plane [1̄100] axis (see Fig. 1) induces the inversion of the heavy hole and split-off hole bands.²⁷ The resulting valence-band maximum has a small effective mass along the k_y direction, leading to increased hole mobility. Using an effective-mass-theory approach, Yeo *et al.* found that for growth in the (10̄10) crystal orientation, strain induced in a GaN quan-

tum well sandwiched between AlGaN layers would lead to a lighter effective mass along the compression direction.²⁸ In recent experiments, Gupta *et al.* realized uniaxial compressive strain of GaN in the basal plane of the wurtzite structure (perpendicular to the [0001] axis, see Fig. 1) by using a fin geometry, while allowing for strain release in the other directions.²⁹ This setup achieved a 25%-50% reduction in sheet resistance of *p*-type GaN along the compressive uniaxial strain direction. Using the *ab initio* Boltzmann transport equation (*aiBTE*), Poncé *et al.* showed that imposing tensile biaxial strain in the (0001) plane, resulting in 2% compression along the *c* axis, raises the split-off band above the heavy- and light-hole bands, thereby increasing the hole mobility along the same direction by 250%.^{17,18}

In this work, we explore an alternative strategy for improving the hole mobility of GaN via strain engineering. A possible route to inducing in-plane uniaxial strain perpendicular to the GaN crystal *c* ([0001]) axis is via epitaxial growth of GaN on II-IV nitride materials with mismatched lattice parameters. Two candidate materials for this purpose are ZnGeN₂ and MgSiN₂, which crystallize in an orthorhombic lattice with space group Pna2₁. To discuss the relation between the lattice parameters of ZnGeN₂, MgSiN₂, and GaN, we use a common reference frame for the hexagonal and the orthorhombic lattices, as shown in Fig. 1. The correspondence between hexagonal and orthorhombic directions is provided in Table S1.

For ZnGeN₂, a range of values has been reported for the room-temperature (300 K) lattice parameters along the [100] and [010] directions [see Fig. 1(b)]: $a = 6.38\text{--}6.45$ Å and $b = 5.46\text{--}5.52$ Å.^{30,31} We consider the values $a = 6.425$ Å and $b = 5.478$ Å to be representative as averages over the experimentally measured lattice parameters and will proceed to use these to determine strain values. For MgSiN₂, accurate x-ray and neutron diffraction measurements at room temperature in-

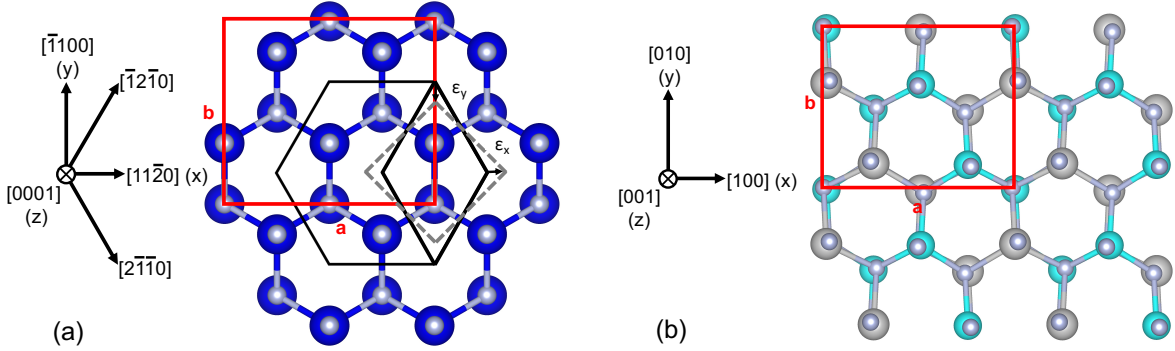


FIG. 1. (a) Crystal structure of GaN, with Ga shown in dark blue and N in silver. The primitive unit cell of GaN is shown as the thick black diamond, and the orthorhombic unit cell is shown in red. The lattice parameters a and b refer to the orthorhombic cell. The deformed gray diamond shows the strain directions (not in scale). We also show how the Cartesian reference frame is aligned with respect to the standard crystallographic directions of the hexagonal lattice. (b) Crystal structure of ZnGeN₂ and MgSiN₂, with Zn or Mg shown in light blue, and Ge or Si in grey. The crystallographic directions of the orthorhombic lattice are aligned with the Cartesian axis.

dicate lattice constants $a = 6.473 \text{ \AA}$ and $b = 5.272 \text{ \AA}$.³²

The lattice parameters of GaN in the orthorhombic cell outlined in Fig. 1(a) are $a = 6.364 \text{ \AA}$ and $b = 5.511 \text{ \AA}$,^{31,33} therefore the epitaxial matching of GaN to ZnGeN₂ and MgSiN₂ will induce a tensile strain ε_x along the a (x) direction, and a compressive strain ε_y along the b (y) direction. For calculations of strained GaN, we impose the strain using the experimental room-temperature lattice parameters of GaN and the II-IV nitrides (see details in the supplementary material). The resulting strain values are listed in Table I. Growth of ZnGeN₂ on GaN has recently been demonstrated via molecular beam epitaxy,³¹ paving the way for the realization of devices based on strained GaN. Growth of GaN on MgSiN₂ or MgSiN₂ on GaN has not yet been explored. The effect of in-plane uniaxial strain on the mobility of GaN has been investigated theoretically using a variety of effective-mass models,^{34–37} but these models predate recent developments in predictive *ab initio* calculations of carrier mobilities,^{17,19,38} hence a study using state-of-the-art computational techniques is warranted.

We perform density functional theory (DFT) calculations, density functional perturbation theory (DFPT) calculations, and Wannier-Fourier interpolation of electronic structure, phonon dispersions, and electron-phonon coupling matrix elements using the Quantum ESPRESSO package,³⁹ the Wannier90 code,⁴⁰ and the EPW code.^{41–44} We use the local density approximation (LDA)^{45,46} and optimized norm-conserving Vanderbilt (ONCV) pseudopotentials.^{47,48} In order to obtain accurate band structures and effective masses, we employ the GW method as implemented in the Yambo code,^{49–51} including spin-orbit coupling in the calculations. The calculation of carrier drift mobility is performed using the *ab initio* Boltzmann transport equation^{52,53} (*aiBTE*) and ultra-dense grids of wavevectors in the Brillouin zone,^{38,54–56} as implemented in the EPW code. A detailed description of the computational setup is provided in the supplementary material.

We perform structural optimization of the unit cell parameters and internal coordinates of unstrained GaN. For strained GaN, we determine the strain configuration in the xy plane us-

TABLE I. Strains along the x and y directions resulting from lattice matching GaN to ZnGeN₂ and MgSiN₂.

	ε_x	ε_y
GaN@ZnGeN ₂ ^{30,31}	0.96%	-0.60%
GaN@MgSiN ₂ ³²	1.72%	-4.33%

ing the experimental lattice parameters of GaN, ZnGeN₂, and MgSiN₂, and we optimize the c parameter as well as the internal coordinates, see Fig. 1. Detailed information about the structural parameters and strain levels considered is reported in Table S1 and Fig. S1. In the following we discuss three systems: unstrained GaN, and GaN strained to match ZnGeN₂ (GaN@ZnGeN₂) or MgSiN₂ (GaN@MgSiN₂) (Table I).

Figures 2(a)-(d) show the valence-band structure of unstrained and strained GaN near the band extremum. In panels (a) and (b) we compare unstrained GaN with GaN@ZnGeN₂, and in panels (c) and (d) we compare unstrained GaN with GaN@MgSiN₂. The reciprocal space lines Γ –X, Γ –Y, and Γ –Z are aligned with the corresponding Cartesian directions in real space, shown in Fig. 1. The strain induces an inversion of the heavy-hole band and of the split-off hole band along the compression direction Γ –Y, leading to a reduced effective mass in the same direction. The energy separation between the inverted bands along this direction is 50 meV for ZnGeN₂, and 320 meV for MgSiN₂. We note that this behavior is only observed for the compression direction, while band inversion does not occur along the directions of tensile strain (Γ –X and Γ –Z).

In Figs. 2(e)–(g) we show maps of the energy of the highest valence band of GaN, GaN@ZnGeN₂, and GaN@MgSiN₂ in the k_x – k_y plane, for $k_z = 0$. Panel (e) shows the expected six-fold symmetry of the band of unstrained GaN. Panels (f) and (g) show that strain reduces this symmetry and the map adopts the symmetries of the orthorhombic structure, with the steepest dispersion and lightest mass along the k_y direction.

To quantify the change in effective masses, we calculate

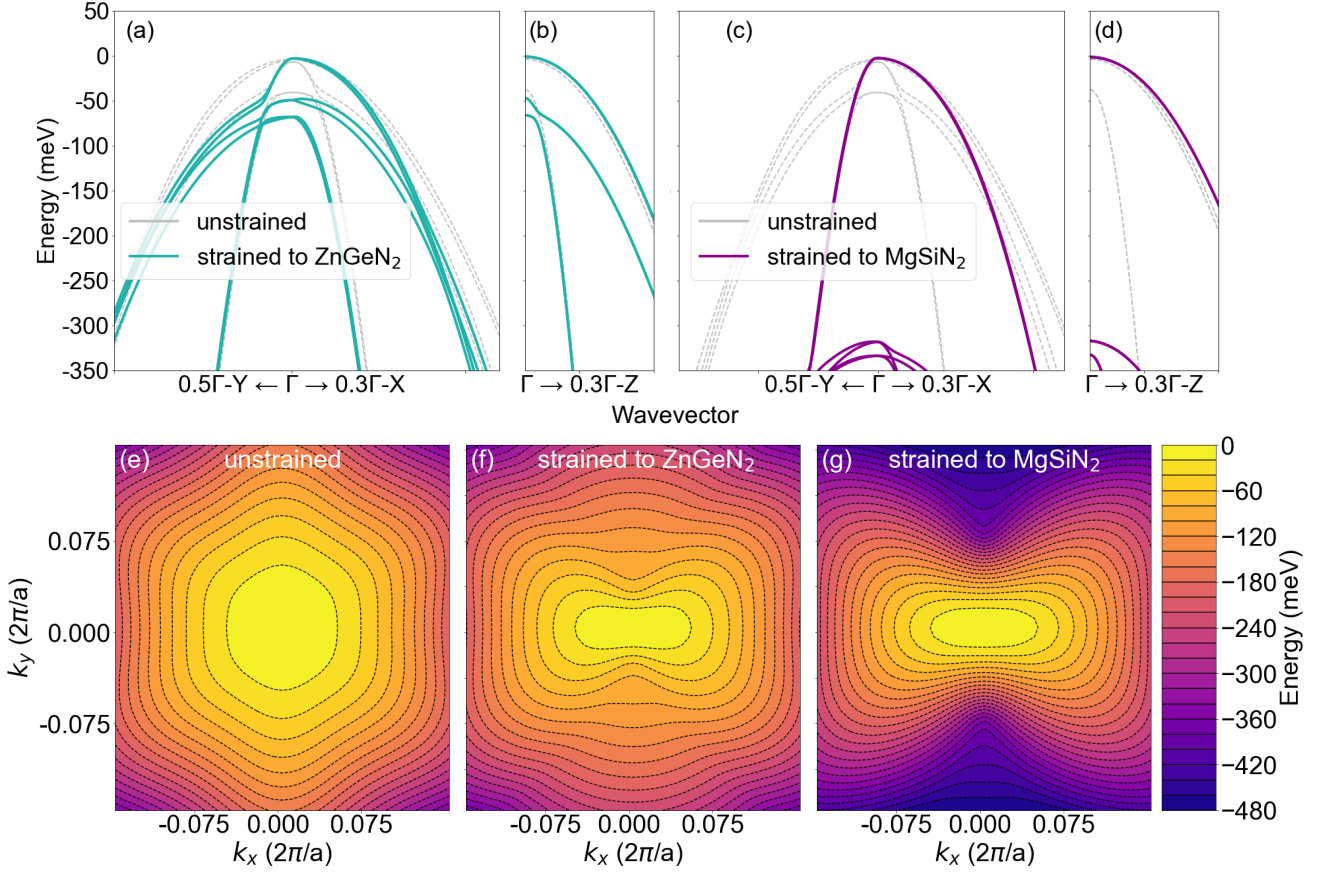


FIG. 2. (a) and (b) Valence-band structure of GaN (grey dashed lines) and GaN@ZnGeN₂ (green solid lines) near the band extremum. (c) and (d) Valence-band structure of GaN (grey dashed lines) and GaN@MgSiN₂ (purple solid lines) near the band extremum. (e) Energy of the highest valence band of GaN vs. k_x and k_y , in a two-dimensional plot with $k_z = 0$. (f) Same setup as in (e), but for GaN@ZnGeN₂. (g) Same setup as in (e), but for GaN@MgSiN₂.

the curvature of the GW bands along the k_x , k_y , and k_z directions using finite differences within 5 meV of the valence-band maximum. The results of these calculations are reported in Table II, and methodological details are provided in the supplementary material. Unstrained GaN exhibits an effective mass $m^* = 0.48 m_e$ along the Γ -X and Γ -Y directions, and $m^* = 1.98 m_e$ along Γ -Z. These values are in agreement with previous GW calculations.¹⁷ In the case of anisotropically strained GaN, we find lighter effective masses along the direction of compression, namely $m^* = 0.21 m_e$ and $m^* = 0.18 m_e$ for GaN@ZnGeN₂ and GaN@MgSiN₂. The electron effective masses can be found in Table S4 in the supplementary material.

We note that we find significant non-parabolicity in the valence band frontier of GaN, as noted in previous theoretical calculations.⁵⁷ In particular, a parabolic dispersion is found only within a 5 meV energy range from the valence band top in unstrained GaN. Below this energy, a band swap occurs and the heavy-hole band becomes the highest valence band. The valence bands of strained GaN@ZnGeN₂ also display non-parabolicity: the bands within 50 meV of the maximum are split-off holes with low effective masses, while the bands below 50 meV are the heavy holes. A detailed analysis of

TABLE II. Directional hole effective masses of GaN, GaN@ZnGeN₂, and GaN@MgSiN₂. We report the hole effective masses for the highest valence band in each case. This mass corresponds to the heavy holes for GaN, and to the split-off holes for GaN@ZnGeN₂ and GaN@MgSiN₂. All masses are in units of the free electron mass.

	Direction	GaN	GaN@ZnGeN ₂	GaN@MgSiN ₂
Holes	x	0.48	1.57	1.62
	y	0.48	0.21	0.18
	z	1.98	2.08	2.30

the variation of the effective mass with energy is reported in Fig. S2.

We also checked the effect of strain on the phonon dispersion relations of GaN. Fig. S3 shows the change of the phonon band structures from unstrained GaN to GaN@ZnGeN₂ and GaN@MgSiN₂. As expected, the only significant changes are observed for GaN@MgSiN₂, which carries the largest strain. In this case we find an 11% reduction in group velocity of transverse acoustic phonons along the compression direction, and a 2.5% increase in the longitudinal optical phonon energy.

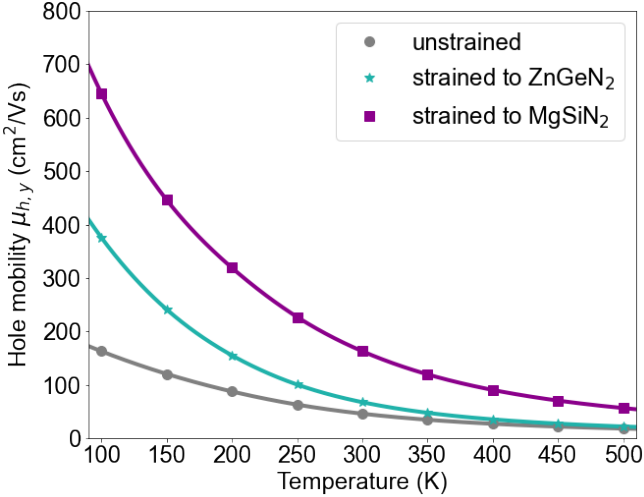


FIG. 3. Hole mobility in the y direction as a function of temperature, calculated with the full *aiBTE*, for unstrained GaN (grey), GaN@ZnGeN₂ (teal), and GaN@MgSiN₂ (magenta).

Our *aiBTE* calculations yield room-temperature hole mobilities along the x and y directions $\mu_x = \mu_y = 46$ cm²/Vs, and z direction $\mu_z = 42$ cm²/Vs for unstrained GaN, in agreement with previous calculations.¹⁷ Our results slightly exceed the mobility of 31 cm²/Vs measured on *p*-type, ultra-low defect-density GaN samples.²⁴ Upon application of strain, the mobility increases to $\mu_y = 67$ cm²/Vs for GaN@ZnGeN₂ (47% increase) and to $\mu_y = 163$ cm²/Vs for GaN@MgSiN₂ (255% increase). Temperature-dependent mobilities for all three cases are shown in Fig. 3.

Along the x and z directions, where the material experiences tensile strain, the hole mobility is only slightly changed: in the case of GaN@ZnGeN₂, the mobility decreases by 12% along the x direction and by 1% along the z direction; in the case of GaN@MgSiN₂, the mobility increases by 4% along x and decreases by 7% along z . The temperature-dependent mobilities along the x and z directions are shown in Figs. S4 and S5. We have also analyzed electron mobilities, but due to the largely isotropic nature of the conduction band, the values for GaN@ZnGeN₂ and GaN@MgSiN₂ show only minor deviations from the values in unstrained GaN (see supplementary material).

The mobility is mostly dictated by the band dispersions, which have been discussed above, and the carrier scattering rates. We analyze the most representative electron-phonon scattering rates⁵⁸ by considering holes located at $3k_B T/2 = 39$ meV below the valence-band maximum, with $T = 300$ K. To do so, we perform a spectral decomposition of the angular-averaged scattering rate by phonon energy (see Fig. S6). For unstrained and strained GaN the trends are consistent: we find that 80% of the scattering rate originates from acoustic phonon scattering, and in particular piezoacoustic scattering. Scattering by longitudinal-optical phonons account for 15% of the total scattering rate, and scattering by transverse-optical phonons accounts for the remaining 5%. The scattering rates as a function of energy from the valence band edge are re-

TABLE III. Effective masses m_y^* , scattering rates $1/\tau$, and mobilities in the compressive strain direction (y) for holes in GaN, GaN@ZnGeN₂, and GaN@MgSiN₂. The scattering rates are evaluated at room temperature for holes with energy $3k_B T/2$ below the top of the valence band. The Drude mobility $\mu_{h,y} = e\tau/m_{h,y}^*$ is only an approximation, and is compared with the accurate *aiBTE* mobility resulting from full Boltzmann transport calculations including all electron-phonon scattering processes.

	GaN	GaN@ZnGeN ₂	GaN@MgSiN ₂
m_y^* (m_e)	0.48	0.21	0.18
$1/\tau$ (THz)	54.0	59.2	43.9
$\mu_{h,y}$ (cm ² /Vs)	Drude	68	141
	<i>aiBTE</i>	46	67
$\mu_{h,y}$ (cm ² /Vs)	GaN	GaN@ZnGeN ₂	GaN@MgSiN ₂

ported in Supplemental Fig. S7, and their values at $3k_B T/2$ are reported in Table III. We see that the scattering rates are much less sensitive to strain than the effective masses, therefore the main source of mobility enhancement is the decrease in the hole mass.

It is instructive to compare our mobility in the compressive y direction from *aiBTE* calculations with the trends that one obtains from a simple Drude model, with values reported in Table III. While the trends in the Drude mobilities are similar to the *aiBTE* results, the Drude values are off by a factor of two. We attribute this to the fact that the valence-band structures of GaN@ZnGeN₂ and GaN@MgSiN₂ display significant anisotropy and a complex, non-parabolic structure; a first-principles treatment is therefore required to accurately describe hole transport in strained GaN systems.

The strain values for GaN@ZnGeN₂ are modest and should allow for pseudomorphic growth of GaN layers of sufficient thickness for device structures. The GaN@MgSiN₂ values are probably too large to allow for growth of device structures; we are including MgSiN₂ to establish trends, and in the eventuality that partially relaxed or alloyed layers based on MgSiN₂ could be used in structures with a smaller mismatch. Given that the mobility enhancement in GaN@ZnGeN₂ is modest, and that the more appealing GaN@MgSiN₂ may be difficult to realize due to the high strain, we also considered the possibility of modifying the lattice parameters of ZnGeN₂ through alloying. In this context, we assess the potential of hypothetical solid solutions of $Zn_{1-x}Ge_{1-x}Mg_xSi_xN_2$. Figure 4(a) shows how the band structure of GaN evolves under increasing strain from $x = 0$ to $x = 1$. As expected, with increasing compressive strain the heavy hole band is further lowered in energy, thereby increasing the energy separation between the split-off holes and the heavy holes, as shown in Fig. 4(b). However, while the energy separation between split-off holes and heavy holes is linear in the strain, we find that the hole mobility varies nonlinearly, and tends to saturate near $x = 0.25$. At $x = 0.25$ the hole mobility in the y direction is already as high as 121 cm²/Vs, which is more than 160% higher than in unstrained GaN.

Finally, the effects of including the long-range quadrupole moment, omitted in this work, in interpolating the

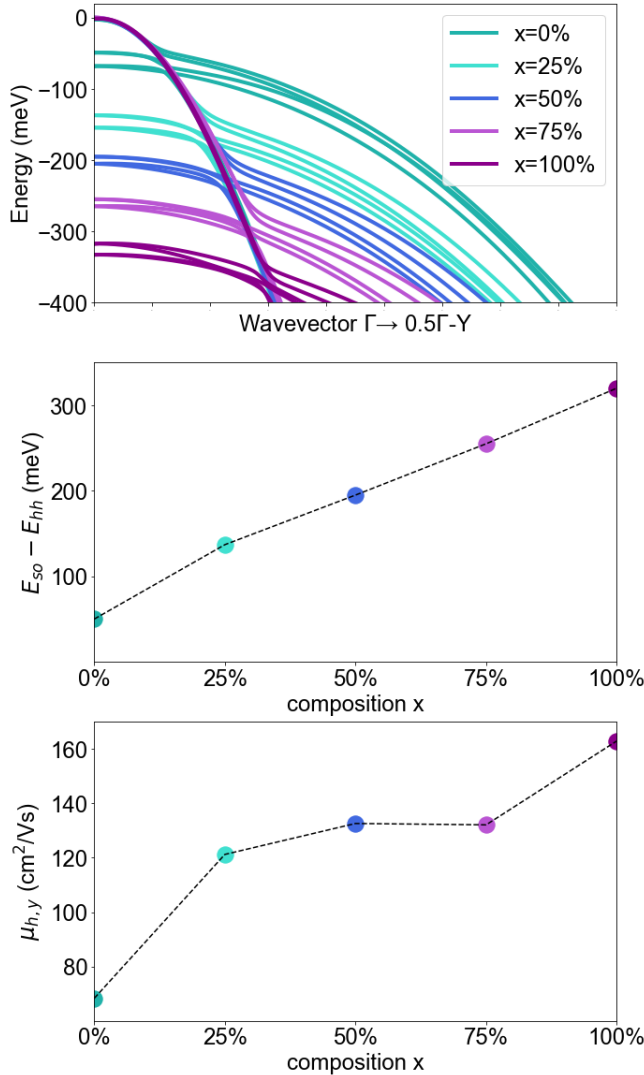


FIG. 4. (a) Valence-band structures of GaN grown on hypothetical solid solutions of $Zn_{1-x}Ge_{1-x}Mg_xSi_xN_2$, which correspond to ZnGeN₂ and MgSiN₂ in the limiting cases of $x = 0$ and $x = 1$, respectively. (b) Energy separation between the split-off hole band and the heavy hole band at the zone center, as a function of x in $Zn_{1-x}Ge_{1-x}Mg_xSi_xN_2$. (c) Calculated room-temperature hole mobility of strained GaN along the y direction, as a function of alloy composition x .

electron-phonon matrix elements in GaN have been previously explored.^{19,55,56,59} It was shown that the mobility of GaN increases from $45 \text{ cm}^2/\text{Vs}$ to $55 \text{ cm}^2/\text{Vs}$ when including quadrupole corrections (22% increase). We demonstrate that the scattering physics across strain states remains consistent, and the increase in hole mobilities is driven by the change in band dispersions under strain. The inclusion of the long-range quadrupole would thus scale the mobilities upwards, but we anticipate the trends with strain to remain the same. We have additionally tested the influence of including long-range quadrupoles moments in the interpolation on the calculated hole mobility μ_y in unstrained GaN and found

an increase to $53 \text{ cm}^2/\text{Vs}$ from $47 \text{ cm}^2/\text{Vs}$, in agreement with previous studies.

In summary, using state-of-the-art first-principles calculations and the *ab initio* Boltzmann transport equation, we investigated the possibility of increasing the room-temperature hole mobility of GaN through anisotropic in-plane strain via pseudomorphic epitaxial growth on ZnGeN₂ and MgSiN₂. We found that GaN@ZnGeN₂ can lead to an increase in the hole mobility along the direction of compression from $46 \text{ cm}^2/\text{Vs}$ in unstrained GaN to $76 \text{ cm}^2/\text{Vs}$, and GaN@MgSiN₂ can increase the mobility up to $163 \text{ cm}^2/\text{Vs}$. Due to the nonlinear dependence of mobility on strain, a hypothetical solid solution of 25% MgSiN₂ added to ZnGeN₂ would already increase the hole mobility to $121 \text{ cm}^2/\text{Vs}$. Beyond strain engineering *p*-channel GaN devices, growth of effectively uniaxial compressed GaN on II-IV nitrides could pose a promising route for engineering monolithic GaN complementary metal–oxide–semiconductor (CMOS) devices. We hope that the present study will motivate renewed experimental efforts toward the realization of high-mobility *p*-type GaN.

This research is supported by the Computational Materials Sciences Program funded by the U.S. Department of Energy (DOE), Office of Science, Basic Energy Sciences BES), under Award No. DE-SC0020129 (J.L.: calculations and data analysis, manuscript preparation; F.G.: project supervision, manuscript preparation). S.P. acknowledges support from the F.R.S.-FNRS and the Consortium des Équipements de Calcul Intensif (CÉCI). Work by N.L.A. was supported by the Army Research Office (W911NF-16-1-0538). Work by C.G.VdW. was supported by the US DOE, Office of Science, BES, under Award No. DE-SC0010689. The authors acknowledge the Texas Advanced Computing Center (TACC) at The University of Texas at Austin for providing HPC resources, including the Frontera and Lonestar5 systems, that have contributed to the research results reported within this paper. URL: <http://www.tacc.utexas.edu>. This research used resources of the National Energy Research Scientific Computing Center, a DOE Office of Science User Facility supported by the Office of Science of the U.S. Department of Energy under Contract No. DE-AC02-05CH11231. Finally, this material is based upon work supported by the National Science Foundation under OAC Grant No. 2103991 (software development, J.L.).

I. SUPPLEMENTARY MATERIAL

Supporting information, including full calculation details and additional data, can be found in the Supplementary Materials document.

CONFLICTS OF INTEREST

The authors have no conflicts of interest to disclose

DATA AVAILABILITY STATEMENT

The data that support the findings of this study are available from the corresponding author upon reasonable request.

- ¹D. W. Runton, B. Trabert, J. B. Shealy, and R. Vetry, "History of GaN: high-power rf gallium nitride (GaN) from infancy to manufacturable process and beyond," *IEEE Microw. Mag* **14**, 82–93 (2013).
- ²Y. Zhang, A. Zubair, Z. Liu, M. Xiao, J. Perozek, Y. Ma, and T. Palacios, "GaN FinFETs and trigate devices for power and RF applications: review and perspective," *Semicond. Sci. Technol.* **36**, 054001 (2021).
- ³H. Amano, Y. Baines, E. Beam, M. Borga, T. Bouchet, P. R. Chalker, M. Charles, K. J. Chen, N. Chowdhury, R. Chu, C. D. Santi, M. M. D. Souza, S. Decoutere, L. D. Cioccio, B. Eckardt, T. Egawa, P. Fay, J. J. Freedman, L. Guido, O. Häberlen, G. Haynes, T. Heckel, D. Hemakumara, P. Houston, J. Hu, M. Hua, Q. Huang, A. Huang, S. Jiang, H. Kawai, D. Kinzer, M. Kuball, A. Kumar, K. B. Lee, X. Li, D. Marcon, M. März, R. McCarthy, G. Meneghesso, M. Meneghini, E. Morvan, A. Nakajima, E. M. S. Narayanan, S. Oliver, T. Palacios, D. Piedra, M. Plissonnier, R. Reddy, M. Sun, I. Thayne, A. Torres, N. Trivellin, V. Unni, M. J. Uren, M. V. Hove, D. J. Wallis, J. Wang, J. Xie, S. Yagi, S. Yang, C. Youtsey, R. Yu, E. Zanoni, S. Zeltner, and Y. Zhang, "The 2018 GaN power electronics roadmap," *J. Phys. D Appl. Phys.* **51**, 163001 (2018).
- ⁴S. Nakamura, M. Senoh, and T. Mukai, "p-GaN/n-InGaN/n-GaN double-heterostructure blue-light-emitting diodes," *Jpn. J. Appl. Phys.* **32**, L8–L11 (1993).
- ⁵S. Nakamura, M. Senoh, N. Iwasa, and S. Nagahama, "High-brightness InGaN blue, green and yellow light-emitting diodes with quantum well structures," *Jpn. J. Appl. Phys.* **34**, L797–L799 (1995).
- ⁶G. Li, W. Wang, W. Yang, Y. Lin, H. Wang, Z. Lin, and S. Zhou, "GaN-based light-emitting diodes on various substrates: a critical review," *Rep. Prog. Phys.* **79**, 056501 (2016).
- ⁷A. S. Barker and M. Illegems, "Infrared lattice vibrations and free-electron dispersion in GaN," *Phys. Rev. B* **7**, 743–750 (1973).
- ⁸O. Madelung, ed., *Semiconductors: group IV elements and III-V compounds* (Springer-Verlag Berlin Heidelberg, 1991).
- ⁹S. Wu, V. Adivarahan, M. Shatalov, A. Chitnis, W.-H. Sun, and M. A. Khan, "Micro-pixel design milliwatt power 254 nm emission light emitting diodes," *Jpn. J. Appl. Phys.* **43**, L1035–L1037 (2004).
- ¹⁰Y. Taniyasu, M. Kasu, and T. Makimoto, "An aluminium nitride light-emitting diode with a wavelength of 210 nanometres," *Nature* **441**, 325–328 (2006).
- ¹¹R. A. Arif, Y.-K. Ee, and N. Tansu, "Polarization engineering via staggered InGaN quantum wells for radiative efficiency enhancement of light emitting diodes," *Appl. Phys. Lett.* **91**, 091110 (2007).
- ¹²C. J. Neufeld, N. G. Toledo, S. C. Cruz, M. Iza, S. P. DenBaars, and U. K. Mishra, "High quantum efficiency InGaN/GaN solar cells with 2.95 eV band gap," *Appl. Phys. Lett.* **93**, 143502 (2008).
- ¹³S. Nakamura, T. Mukai, and M. Senoh, "Si- and Ge-doped GaN films grown with GaN buffer layers," *Jpn. J. Appl. Phys.* **31**, 2883–2888 (1992).
- ¹⁴W. Götz, N. M. Johnson, C. Chen, H. Liu, C. Kuo, and W. Imler, "Activation energies of Si donors in GaN," *Appl. Phys. Lett.* **68**, 3144–3146 (1996).
- ¹⁵W. Götz, L. T. Romano, J. Walker, N. M. Johnson, and R. J. Molnar, "Hall-effect analysis of GaN films grown by hydride vapor phase epitaxy," *Appl. Phys. Lett.* **72**, 1214–1216 (1998).
- ¹⁶E. C. H. Kyle, S. W. Kaun, P. G. Burke, F. Wu, Y.-R. Wu, and J. S. Speck, "High-electron-mobility GaN grown on free-standing GaN templates by ammonia-based molecular beam epitaxy," *J. Appl. Phys.* **115**, 193702 (2014).
- ¹⁷S. Poncé, D. Jena, and F. Giustino, "Hole mobility of strained GaN from first principles," *Phys. Rev. B* **100**, 085204 (2019).
- ¹⁸S. Poncé, D. Jena, and F. Giustino, "Route to high hole mobility in GaN via reversal of crystal-field splitting," *Phys. Rev. Lett.* **123**, 096602 (2019).
- ¹⁹V. A. Jhalani, J.-J. Zhou, J. Park, C. E. Dreyer, and M. Bernardi, "Piezoelectric electron-phonon interaction from ab initio dynamical quadrupoles: impact on charge transport in wurtzite GaN," *Phys. Rev. Lett.* **125**, 136602 (2020).
- ²⁰M. Rubin, N. Newman, J. S. Chan, T. C. Fu, and J. T. Ross, "P-type gallium nitride by reactive ion-beam molecular beam epitaxy with ion implantation, diffusion, or coevaporation of Mg," *Appl. Phys. Lett.* **64**, 64–66 (1994).
- ²¹P. Kozodoy, S. Keller, S. DenBaars, and U. Mishra, "MOVPE growth and characterization of Mg-doped GaN," *J. Cryst. Growth* **195**, 265–269 (1998).
- ²²P. Kozodoy, H. Xing, S. P. DenBaars, U. K. Mishra, A. Saxler, R. Perrin, S. Elhamri, and W. C. Mitchel, "Heavy doping effects in Mg-doped GaN," *J. Appl. Phys.* **87**, 1832–1835 (2000).
- ²³Y. Arakawa, K. Ueno, A. Kobayashi, J. Ohta, and H. Fujioka, "High hole mobility p-type GaN with low residual hydrogen concentration prepared by pulsed sputtering," *APL Materials* **4**, 086103 (2016).
- ²⁴M. Horita, S. Takashima, R. Tanaka, H. Matsuyama, K. Ueno, M. Edo, T. Takahashi, M. Shimizu, and J. Suda, "Hall-effect measurements of metalorganic vapor-phase epitaxy-grown p-type homoepitaxial GaN layers with various mg concentrations," *Jpn. J. Appl. Phys.* **56**, 031001 (2017).
- ²⁵M. McLaurin and J. S. Speck, "p-type conduction in stacking-fault-free m-plane gan," *Phys. Status Solidi RRL* **1**, 110–112 (2007).
- ²⁶S. J. Bader, H. Lee, R. Chaudhuri, S. Huang, A. Hickman, A. Molnar, H. G. Xing, D. Jena, H. W. Then, N. Chowdhury, and T. Palacios, "Prospects for wide bandgap and ultrawide bandgap cmos devices," *IEEE Transactions on Electron Devices* **67**, 4010–4020 (2020).
- ²⁷M. Suzuki and T. Uenoyama, "Strain effect on electronic and optical properties of GaN/AlGaN quantum-well lasers," *J. Appl. Phys.* **80**, 6868–6874 (1996).
- ²⁸Y. Yeo, T. Chong, and M. Li, "Effect of the (1010) crystal orientation on the optical gain of wurtzite GaN-AlGaN quantum-well lasers," *IEEE J. Quantum Electron.* **34**, 1270–1279 (1998).
- ²⁹C. Gupta, Y. Tsukada, B. Romanczyk, S. S. Pasayat, D.-A. James, E. Ahmadi, S. Keller, and U. K. Mishra, "First demonstration of improvement in hole conductivity in c-plane III-nitrides through application of uniaxial strain," *Jpn. J. Appl. Phys.* **58**, 030908 (2019).
- ³⁰E. W. Blanton, K. He, J. Shan, and K. Kash, "Characterization and control of ZnGeN₂ cation lattice ordering," *J. Cryst. Growth* **461**, 38–45 (2017).
- ³¹M. B. Tellekamp, C. L. Melamed, A. G. Norman, and A. Tamboli, "Heteroepitaxial integration of ZnGeN₂ on GaN buffers using molecular beam epitaxy," *Cryst. Growth Des.* **20**, 1868–1875 (2020).
- ³²R. Bruls, H. Hintzen, R. Metselaar, and C.-K. Loong, "Anisotropic thermal expansion of MgSiN₂ from 10 to 300K as measured by neutron diffraction," *J. Phys. Chem. Solids* **61**, 1285–1293 (2000).
- ³³W. Gian, M. Skowronski, and G. S. Rohrer, "Structural defects and their relationship to nucleation of GaN thin films," *MRS Proceedings* **423**, 475 (1996).
- ³⁴D. L. Rode and D. K. Gaskill, "Electron hall mobility of n-GaN," *Appl. Phys. Lett.* **66**, 1972–1973 (1995).
- ³⁵D. C. Look, D. C. Reynolds, J. W. Hemsky, J. R. Sizelove, R. L. Jones, and R. J. Molnar, "Defect donor and acceptor in GaN," *Phys. Rev. Lett.* **79**, 2273–2276 (1997).
- ³⁶D. C. Look and R. J. Molnar, "Degenerate layer at GaN/sapphire interface: influence on hall-effect measurements," *Appl. Phys. Lett.* **70**, 3377–3379 (1997).
- ³⁷I. M. Abdel-Motaleb and R. Y. Korotkov, "Modeling of electron mobility in GaN materials," *J. Appl. Phys.* **97**, 093715 (2005).
- ³⁸S. Poncé, E. R. Margine, and F. Giustino, "Towards predictive many-body calculations of phonon-limited carrier mobilities in semiconductors," *Phys. Rev. B* **97**, 121201 (2018).
- ³⁹P. Giannozzi, O. Andreussi, T. Brumme, O. Bunau, M. B. Nardelli, M. Calandra, R. Car, C. Cavazzoni, D. Ceresoli, M. Cococcioni, N. Colonna, I. Carnimeo, A. D. Corso, S. de Gironcoli, P. Delugas, R. A. DiStasio, A. Ferretti, A. Floris, G. Fratesi, G. Fugallo, R. Gebauer, U. Gerstmann, F. Giustino, T. Gorni, J. Jia, M. Kawamura, H.-Y. Ko, A. Kokalj, E. Küçükbenli, M. Lazzeri, M. Marsili, N. Marzari, F. Mauri, N. L. Nguyen, H.-V. Nguyen, A. O. de-la Roza, L. Paulatto, S. Poncé, D. Rocca, R. Sabatini, B. Santra, M. Schlipf, A. P. Seitsonen, A. Smogunov, I. Timrov, T. Thonhauser, P. Umari, N. Vast, X. Wu, and S. Baroni, "Advanced capabilities for materials modelling with quantum ESPRESSO," *J. Phys. Condens. Matter* **29**, 465901 (2017).
- ⁴⁰A. A. Mostofi, J. R. Yates, G. Pizzi, Y.-S. Lee, I. Souza, D. Vanderbilt, and N. Marzari, "An updated version of wannier90: A tool for obtaining maximally-localised Wannier functions," *Comput. Phys. Commun.* **185**, 2309–2310 (2014).

- ⁴¹F. Giustino, M. L. Cohen, and S. G. Louie, “Electron-phonon interaction using Wannier functions,” Phys. Rev. B **76**, 165108 (2007).
- ⁴²J. Noffsinger, F. Giustino, B. D. Malone, C.-H. Park, S. G. Louie, and M. L. Cohen, “Epw: A program for calculating the electron–phonon coupling using maximally localized Wannier functions,” Comput. Phys. Commun. **181**, 2140–2148 (2010).
- ⁴³C. Verdi and F. Giustino, “Fröhlich electron-phonon vertex from first principles,” Phys. Rev. Lett. **115**, 176401 (2015).
- ⁴⁴S. Poncé, E. Margine, C. Verdi, and F. Giustino, “EPW: electron–phonon coupling, transport and superconducting properties using maximally localized Wannier functions,” Comp. Phys. Comm. **209**, 116 – 133 (2016).
- ⁴⁵D. M. Ceperley and B. J. Alder, “Ground state of the electron gas by a stochastic method,” Phys. Rev. Lett. **45**, 566–569 (1980).
- ⁴⁶J. P. Perdew and A. Zunger, “Self-interaction correction to density-functional approximations for many-electron systems,” Phys. Rev. B **23**, 5048–5079 (1981).
- ⁴⁷D. R. Hamann, “Optimized norm-conserving vanderbilt pseudopotentials,” Phys. Rev. B **88**, 085117 (2013).
- ⁴⁸M. Schlipf and F. Gygi, “Optimization algorithm for the generation of oncv pseudopotentials,” Computer Physics Communications **196**, 36–44 (2015).
- ⁴⁹A. Marini, C. Hogan, M. Grüning, and D. Varsano, “yambo: an ab initio tool for excited state calculations,” Comput. Phys. Commun. **180**, 1392–1403 (2009).
- ⁵⁰D. Sangalli, A. Ferretti, H. Miranda, C. Attaccalite, I. Marri, E. Cannuccia, P. Melo, M. Marsili, F. Paleari, A. Marrazzo, G. Prandini, P. Bonfà, M. O. Atambo, F. Affinito, M. Palummo, A. Molina-Sánchez, C. Hogan, M. Grüning, D. Varsano, and A. Marini, “Many-body perturbation theory calculations using the yambo code,” J. Phys. Condens. Matter **31**, 325902 (2019).
- ⁵¹R. W. Godby and R. J. Needs, “Metal-insulator transition in kohn-sham theory and quasiparticle theory,” Phys. Rev. Lett. **62**, 1169–1172 (1989).
- ⁵²W. Li, “Electrical transport limited by electron-phonon coupling from Boltzmann transport equation: an ab initio study of Si, Al, and MoS₂,” Phys. Rev. B **92**, 075405 (2015).
- ⁵³G. K. Madsen, J. Carrete, and M. J. Verstraete, “Boltztrap2, a program for interpolating band structures and calculating semi-classical transport coefficients,” Comput. Phys. Commun. **231**, 140–145 (2018).
- ⁵⁴S. Poncé, W. Li, S. Reichardt, and F. Giustino, “First-principles calculations of charge carrier mobility and conductivity in bulk semiconductors and two-dimensional materials,” Rep. Prog. Phys. **83**, 036501 (2020).
- ⁵⁵S. Poncé, F. Macheda, E. R. Margine, N. Marzari, N. Bonini, and F. Giustino, “First-principles predictions of Hall and drift mobilities in semiconductors,” Phys. Rev. Research **3**, 043022 (2021).
- ⁵⁶G. Brunin, H. P. C. Miranda, M. Giantomassi, M. Royo, M. Stengel, M. J. Verstraete, X. Gonze, G.-M. Rignanese, and G. Hautier, “Electron-phonon beyond Fröhlich: dynamical quadrupoles in polar and covalent solids,” Phys. Rev. Lett. **125**, 136601 (2020).
- ⁵⁷P. Rinke, M. Winkelkemper, A. Qteish, D. Bimberg, J. Neugebauer, and M. Scheffler, “Consistent set of band parameters for the group-iii nitrides aln, gan, and inn,” Phys. Rev. B **77**, 075202 (2008).
- ⁵⁸S. Poncé, M. Schlipf, and F. Giustino, “Origin of low carrier mobilities in halide perovskites,” ACS Energy Letters **4**, 456–463 (2019).
- ⁵⁹J. Park, J.-J. Zhou, V. A. Jhalani, C. E. Dreyer, and M. Bernardi, “Long-range quadrupole electron-phonon interaction from first principles,” Phys. Rev. B **102**, 125203 (2020).